A COMPARISON OF INDIVIDUAL AND POPULATION-DERIVED VASCULAR INPUT FUNCTIONS FOR QUANTITATIVE DCE-MRI IN RATS

By

David Andrew Hormuth, II

Thesis

Submitted to the Faculty of the

School of Engineering of Vanderbilt University

in partial fulfillment of the requirements

for the degree of

MASTER OF SCIENCE

in

Biomedical Engineering

December, 2012

Nashville, Tennessee

Approved:

Professor Thomas E. Yankeelov

Professor Mark D. Does

ACKNOWLEDGEMENTS

I would like to acknowledge and thank the sources of funding for this project: the National Cancer Institute (CA138599, P30CA068485, R01CA138599, 2R25CA092043, and NCI R25CA136440) and the National Institute of Biomedical Imaging and Bioengineering (EB001744). Additionally I would like to thoroughly thank Dr. Jack Skinner, Ph.D. for collecting the data and for discussions and guidance on this project in particular, and graduate school in general. Thanks to Mark Does for advising and teaching me during my first year of graduate school and for challenging me during the "Magnetic Resonance Imaging Methods" course. I would also like to thank Tom Yankeelov, for advising me throughout this project, further fueling my interest in cancer imaging research, and providing some levity to graduate school.

I would also like to acknowledge and thank my family, my friends, and my 12th South community group for listening and encouraging me throughout my project. Finally, I would like to thank my wife, Jamie Hormuth, for being my companion and supporting me throughout this project, graduate school, and everywhere else.

TABLE OF CONTENTS

LIST OF TABLES

LIST OF FIGURES

CHAPTER I

INTRODUCTION

Imaging Angiogenesis

Once avascular tumor volumes reach approximately 1-2 mm^3 further growth is no longer supported by passive diffusion of nutrients, but requires the recruitment of new vasculature to the tumor mass (1). The recruitment of new vasculature, or angiogenesis, is a believed to be a characteristic trait of nearly all malignant cancers (2). Angiogenesis in a non-pathological state typically results in the formation of normal vasculature, hierarchically organized from large (arteries) to small (capillaries), whereas in pathological states the resulting vasculature is often fragile, leaky, poorly organized, and contains incomplete vessel connections (3). The differences between healthy and abnormal vasculature is one aspect that can be investigated through magnetic resonance imaging (MRI).

Dynamic contrast enhanced magnetic resonance imaging (DCE-MRI) is an imaging technique that can be used to investigate vascular properties of tumors including, for example, blood vessel perfusion and permeability, blood volume, and the extravascular extracellular volume fraction. DCE-MRI probes these characteristics through analysis of dynamic voxel or region of interest (ROI) signal-intensity curves obtained before, during, and after injection of a paramagnetic contrast agent (CA) such as gadopentetate dimeglumine, Gd-DTPA, (Magnevist, Wayne NJ). In healthy vasculature Gd-DTPA predominantly remains within the vessel and is cleared by the kidneys. However, in abnormal vasculature with highly permeable vessel walls, it leaks into the

surrounding tissue space. As the CA travels through the vasculature and extravasates into tissue, the local T_1, T_2, and T_2^* are shortened, to a degree depending on the local concentration of CA thereby resulting in a change in the measured signal-intensity. Time dependent variations of the signal-intensity curve are related to local physiological properties (e.g., vessel wall permeability, blood flow, blood volume, and extravascular space) which can be investigated through pharmacokinetic modeling (4) making it a valuable tool in preclinical and clinical studies of, for example, anti-angiogenic treatments (5).

DCE-MRI data can be analyzed qualitatively, for example, observing tissue enhancement after CA injection to delineate tumor tissue from normal tissue, or quantitatively to extract values describing CA uptake or tumor characteristics. One class of semi-quantitative approaches that does not require modeling of CA kinetics are measures such as wash-in rate and the initial area under the curve (iAUC). The wash-in rate is defined as the maximum slope between injection of the CA and the peak CA intensity, and has been used to distinguish the early enhancement of tumor tissue from healthy tissue (6). Similarly, iAUC measurements have been used to monitor response to anti-angiogenic therapies (7); however, the exact physiological meaning of iAUC remains unclear (8,9). Both wash-in rate and iAUC describe heterogeneity of CA uptake and are a mixed measurement of blood flow, vessel permeability, and interstitial space (9). Individual components of a tumor's vasculature system (e.g., blood flow) can be examined individually through pharmacokinetic modeling of the CA. These pharmacokinetic models describe the uptake, distribution, and clearance of the injected

CA within the body allowing parameters describing the vasculature and tumor environment to be assessed.

Components of Quantitative DCE-MRI

In order to perform quantitative DCE-MRI, three data sets are required of the tissue under investigation: 1) a pre-contrast T_1 map, 2) serial T_1-weighted images obtained before, during, and after the injection of a paramagnetic CA, and 3) the time rate of change of the concentration of CA in a nearby feeding vessel, the so-called vascular input function (VIF). An example VIF, shown in Figure 1, consists of a three distinct characteristics, the rapid wash-in (labeled in the figure as "a"), the peak CA concentration in the plasma (b), and the washout (c), that need to be estimated to describe CA kinetics in blood.

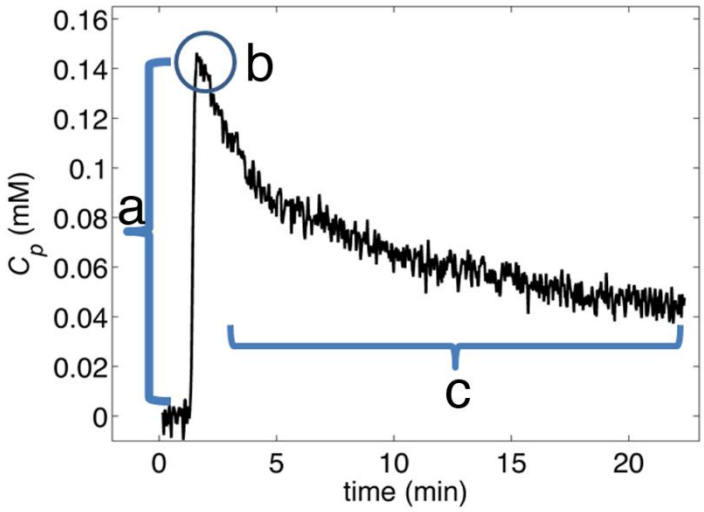

Figure 1: An example VIF acquired from the linguofacial artery in a rat. Following injection of a bolus of a CA, C_p rapidly increases **(a)**, reaches its peak **(b)** concentration during the first pass, and subsequently decreases **(c)** due to distribution and elimination. Point **(a)** represents the rapid wash-in of a bolus of CA

Capturing both the rapid wash-in and the peak concentration require high temporal resolution sampling. The washout portion, however, can be characterized with lower temporal resolution sampling. Accurately estimating these distinct parts in a VIF is extremely challenging, particularly in small animals where small vessel sizes impedes direct VIF measurement.

Measuring the Vascular Input Function

In general, there are three main ways to acquire the VIF: 1) through arterial blood sampling (10), 2) assuming a functional form (e.g., bi-exponential decay) of the VIF (11), and 3) directly from a vessel visible in the imaging data (11-13). Arterial blood sampling is considered the "gold standard" as it allows direct measurement of the CA concentration. However in small animals where the total blood volume is about 2 mL for mice and 16 mL for rats (14), blood sampling is both limited by the number of samples that can be acquired and the achievable temporal resolution. One study by Wedeking *et al* (15) characterizing the plasma distribution of Gd-DTPA in rats acquired 22 samples over 90 minutes. After injection with the CA, the initial rapid rise was sampled every 30-seconds followed by samples spaced 1-minute, 10-minutes, and 15-minutes apart during the washout portion. This study showed that after the CA concentration reaches its peak in the blood its washout can be described by bi-exponential decay. A later study by Nagaraja *et al* (10) in rats compared MRI-measured VIFs to blood sampled VIFs. The MRI-measured VIF was selected from venous blood in the superior sagittal sinus, whereas after the MRI examination the blood sampled VIF was collected from the femoral artery following a second injection of the CA. This study improved the temporal

resolution for the arterial blood sampling by characterizing the rapid rise of CA every 5-seconds and the washout of the CA every 60-seconds, but required blood sampling after the DCE-MRI acquisition. Alternatively, assuming a functional form of the VIF can provide a well characterized and a high signal-to-noise ratio (SNR) curve. A functional form can be generated through fitting a model describing CA kinetics to a VIF acquired through (for example) arterial blood sampling or direct imaging of blood vessels. One common form describes CA washout through bi-exponential decay (15), a modification of which includes two linear fits describing the rapid rise of the CA prior to the peak (16). In this application, the two exponentials refer to the distribution of the CA between compartments and the elimination of CA in the compartments by the kidneys (17). Functional descriptions of the VIF allow high SNR VIFs to be disseminated through publication or generated from low SNR data. An early example using a functional form of the VIF is in Tofts *et al* (17), where VIF data from the literature (18) was fit to a bi-exponential decay and used to characterize CA concentration in plasma. Another functional form derived from an average of a cohort of VIFs consists of a combination of a Gaussian and an exponential modulated by a sigmoid (19). Similar to the bi-exponential decay models it characterizes the rapid rise, peak concentration, and washout; however, this new form allows the recirculation of the CA to be characterized and included in the washout phase. More recently, these functional forms were applied and compared to individual and population-averaged VIFs by McGrath *et al* (11) as a proposed alternative to low temporal resolution or low SNR VIFs. In this study, the bi-exponential form provided the closest agreement to estimates of K^{trans} and v_e derived using a measured VIF. The VIF described by a Gaussian and an exponential modulated

by a sigmoid provided closer agreement for estimates of v_p compared to the bi-exponential model. The closer agreement to v_p obtained by this model was suggested to be a result of the introduction of a recirculation peak into the model, which may be critical in assessing v_p accurately.

The VIF may also be acquired directly from the imaging data if a well-resolved blood pool from a feeding vessel is present within the field of view (FOV). One approach is to include either the heart or a major artery within the field of view (11,20). This can be challenging in small animals where small vessel sizes make it difficult to select blood pools devoid of partial volume effects. In preclinical work, this may restrict tumor implantation sites or require larger FOVs and the use of larger imaging coils. If a major blood pool is not within the FOV of the tumor, interleaving the target tissue (e.g., a tumor) with an additional slice containing the vessel, or through dual coil acquisition of a peripheral artery or vein (21), can provide an imaging derived measure of the VIF. Dual coil approaches typically involve the use of two surface or volume coils to image both the tumor and either the tail or heart. Both interleaving approaches lessen the potential need of a compromise between the desired VIF and tumor locations.

All of these image-based approaches, however, require high temporal resolution acquisitions to capture the VIF's rapid uptake and washout of the CA. Conversely in tissue, CA uptake and washout can be accurately characterized at a lower temporal resolution. Additionally, in pre-clinical cancer studies high spatial resolution is desired to observe tumor heterogeneity. Tumors do not consist of just a single tissue type but consist of multiple tissue types resulting in a range of tumor properties (22,23). These image-based approaches therefore require a technical balance between high spatial and

temporal resolution acquisitions in order to characterize both tumor heterogeneity and the VIF.

Population-Averaged VIF

Two alternative imaging derived approaches that alleviate the technical constraints of acquiring both high spatial and temporal resolution images are the reference region method and the use of a population-averaged VIF. In a reference region analysis, parameters and the signal-intensity time course from a reference tissue are used in pharmacokinetic analysis to calibrate CA uptake in tumors (24). This allows the high temporal resolution acquisition required to characterize the VIF to be replaced by a reference tissue whose CA uptake and washout can be characterized at a lower temporal resolution. Rather than acquire a VIF for each individual subject, some investigators have explored using a population-averaged VIF built from a cohort of subjects and subsequently used for pharmacokinetic analysis (11,19,25-28). Exchanging an individual based VIF with a population-averaged VIF reduces the considerable temporal resolution and SNR restrictions required for individual VIF measurements, thereby potentially allowing improved characterization of the tumor environment. An early investigation by Simpson *et al* (29) in rats on the optimization of VIF acquisition suggested the use of a population-averaged VIF for measuring perfusion. The population-averaged VIF resulted in errors up to 60% when a common dose was used for each rat; however, when rats were injected with a dose proportional to their mass these errors dropped to 20%. These observed errors in perfusion estimates may arise from both experimental (e.g., anesthetic agent, duration of anesthesia, dose per mass) and physiological (e.g., disease state, blood

pressure, heart rate) variations between the individual and the cohort. A study by Pickup *et al* (30) in mice preferred the use of an individual VIF over the population-averaged VIF due to considerable inter-animal variability in the VIF resulting in inconsistencies between parameters derived from both VIFs. (It should be noted, however, that this study included only four mice in the data set.) Contrary to these two studies, Parker *et al* (19) generated a population-averaged VIF from 23 patients (ages ranging from 18-80 years) with advanced cancer and demonstrated that a high-temporal-resolution population VIF had increased sensitivity to therapy induced changes. Following this McGrath *et al (11)* compared (in rats) the repeatability and sensitivity of pharmacokinetic parameters estimated using an individual VIF, a population-averaged VIF, and functional forms fit to the population-averaged VIF. Increased sensitivity and repeatability of model estimates was observed for both the raw data population-averaged VIF and the bi-exponential model fit of this data over the individual VIF. An additional clinical study by Meng *et al* (28) compared the ability of parameters obtained with the population-averaged and the individually acquired VIF to predict prostate cancer biopsy results. No significant difference was observed between predicted biopsy results obtained through either VIF. A more recent study with rats investigated the effect of heart rate on pharmacokinetic parameters extracted using a population-averaged VIF from DCE-CT to those extracted through a reference-region approach (26). No significant difference was observed between the population-averaged VIF and reference region approaches for rats with the same heart rate; however, when heart rate was increased by 30% a 19-43% difference was observed between reference region and the population-averaged VIF. Most recently, a study by Loveless *et al* (27), compared the VIF in mice using two different CAs of

varying molecular weight and reported very high correlation (concordance correlation coefficient > 0.850) for K^{trans} parameters estimated using population and individual VIFs with Gd-DTPA.

Following the work of Loveless *et al* (27), the goal of this study is to perform a careful comparison between individual and population-averaged VIFs derived from a cohort of rats bearing brain tumors. The individual and population based VIFs were used to extract physiologically relevant parameters through DCE-MRI modeling and the resulting parameters were statistically compared at both the voxel and ROI level.

CHAPTER II

EXPERIMENTAL METHODS

Pharmacokinetic Modeling Theory

Pharmacokinetic modeling is a quantitative tool that can be used in the analysis of DCE-MRI data. Through analysis of these data, parameters describing vessel wall permeability, blood flow, blood and extravascular volume fractions can be extracted. A commonly used model, developed by Kety (31) and applied to DCE-MRI (4), consists of two compartments: the concentration of the CA in blood/plasma space (C_p) and the concentration of the CA in tissue space (C_t). The two compartment model, shown in Figure 2, includes two transfer constants describing the exchange of CA between compartments.

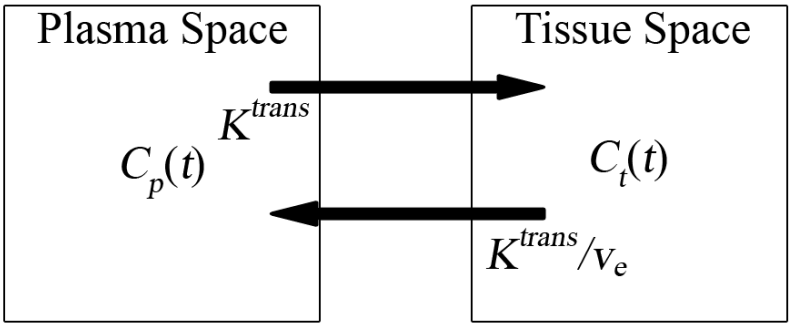

Figure 2: Two compartment model describing concentration of the CA in the plasma space (C_p) and in the (extravascular) tissue space (C_t). Movement between compartments is described by rates K^{trans} and K^{trans}/v_e.

It is straight forward to write down the relevant differential equation describing this situation:

$$\frac{dC_t(t)}{dt} = K^{trans} \times C_p(t) - \left(K^{trans} \Big/ v_e \right) \times C_t(t) \quad . \qquad [1]$$

In words, Eq. [1] describes the time rate of change in C_t as the amount of CA entering C_t from C_p minus the amount of CA leaving C_t and entering C_p. The transfer constant K^{trans} describes the movement of the CA from C_p to C_t, while K^{trans} divided by the extravascular extracellular volume fraction v_e (K^{trans}/v_e) describes the movement of the CA from C_t back to C_p. The physiological meaning of K^{trans} depends on assumptions of tissue characteristics. Tissues where flow is much greater than blood vessel permeability are said to be permeability limited, while areas with highly permeable blood vessels but weak blood flow are flow limited. In tumors, tissues are assumed to be either permeability limited or a combination of both flow and permeability limited. Eq. [1] is a first order ordinary differential equation which can be solved by (for example) the Laplace Transform method to yield:

$$C_t(t) = K^{trans} \times \int_0^t C_p(u) \times e^{-\left(K^{trans}/v_e\right) \times (t-u)} du \qquad [2]$$

Not included in the model displayed in Figure 2 is the effect of a significant vascular component in the region under investigation. Avascular tissues consist of both a cellular and an extracellular component, while vascular tissues consist of a cellular, a vascular, and an extravascular extracellular component. In tumors undergoing neovascularization this vascular space can affect CA pharmacokinetics and, if not

included in the pharmacokinetic model, result in overestimation of K^{trans}. Figure 3 shows an adaptation of Figure 2 to include the vascular component.

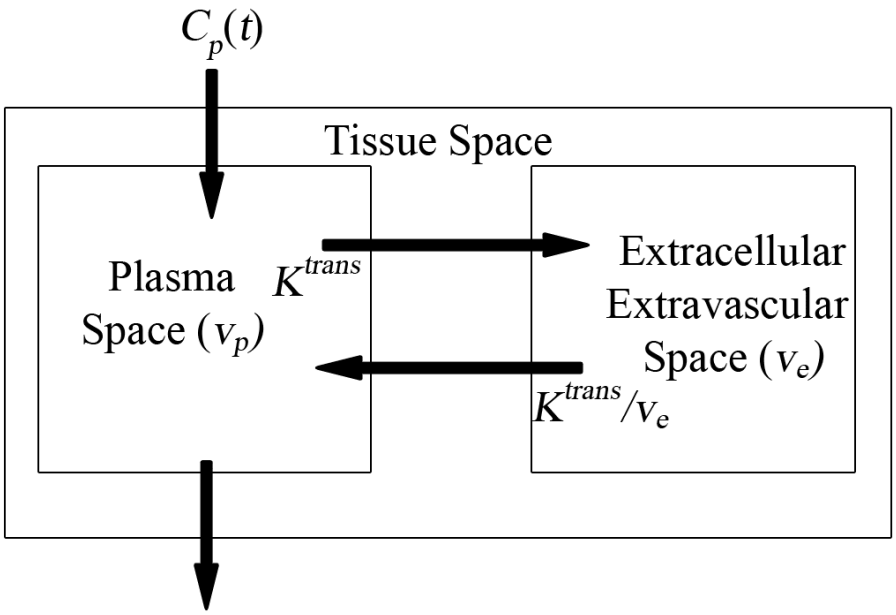

Figure 3: An extension of the model in Figure 2, this model accounts for both a plasma space and an extracellular extravascular space as CA compartments within the tissue space. Here K^{trans} and K^{trans}/v_e describe the movement of CA in between different the two different tissue space components

C_t can now be calculated by adding the concentration of CA in the extracellular extravascular space, Eq. [2], and C_p resulting in Eq. [3]:

$$C_t(t) = K^{trans} \times \int_0^t C_p(u) \times e^{-\left(K^{trans}/v_e\right)\times(t-u)} du + v_p \times C_p(t) \qquad [3]$$

In order to use the Toft's model in Eq. [2] and its extension presented in Eq. [3], to extract pharmacokinetic parameters a T_1 map, a set of T_1-weighted images before, during, and after injection with a CA, and knowledge of the CA kinetics in blood is

needed. Typically changes in local R_1 ($\equiv 1/T_1$) due to the addition of a paramagnetic CA can be estimated *via* Eq. [4]:

$$R_1 = r_1 \times [CA] + R_{10}, \quad [4]$$

where the concentration of the CA, [*CA*], its relaxivity, r_1, and the pre-contrast R_1 value, R_{10}, is known. However, in DCE-MRI the concentration of the CA in a given voxel or ROI is not known *a priori* and must be determined. Additionally, Eq. [4] is adjusted to reflect only the extravascular extracellular space (v_e) of the tissue and plasma compartments. Rearranging to solve Eq. [4] for C_t yields:

$$C_t(t) = \frac{R_1(t) - R_{10}}{r_1 \times v_e} \quad [5]$$

Similarly, after rearranging to solve for C_p and excluding the cellular volume, or hematocrit (h), Eq. [4] becomes:

$$C_p(t) = \frac{R_1(t) - R_{10}}{r_1 \cdot (1-h)} \quad [6]$$

Ideally T_1 maps ($\equiv 1/R_{10}$) would be acquired at each time point, however, T_1 changes too rapidly for this approach to be feasible. Instead a baseline T_1 map is acquired to calibrate future changes as observed in the set of serial T_1-weighted images. Using a spoiled gradient echo sequence a R_1 time course can be extracted from a signal-intensity curve *via* Eqs. [7] and [8]:

$$R_1(t) = \frac{1}{TR} \times \ln\left[\frac{S_0 \times \sin\alpha - S(t) \times \cos\alpha}{S_0 \times \sin\alpha - S(t)}\right], \quad [7]$$

where TR and α are scan parameters, S_0 was defined as

$$S_0 = S_{pc} \times \left[\frac{1 - e^{-TR \times R_{10}} \times \cos\alpha}{\left(1 - e^{-TR \times R_{10}}\right) \times \sin\alpha} \right], \quad [8]$$

where S_{pc} is the pre-contrast signal intensity. By extracting dynamic signal intensity data of voxel or ROI within tumor tissue C_t can be determined using Eqs. [5, 7-8] and using the VIF C_p can be determined using Eqs. [6-8].

In this work, both the standard (ST) model, Eq.[2], and the extended (EX) model, Eq. [3], are used in evaluating DCE-MRI data sets. These models provide insight into both predominately avascular and vascular tissues. The definition of the tissue space in the ST model assumes that either the tumor tissue is avascular or has a negligible vascular component. However, if the vascular component of tissue space is significant, as is the case in many tumors undergoing neovascularization, the EX model may be more accurately describe C_t.

Animal Model

Female Sprague-Dawley rats (n = 8, 234–270 g) were anesthetized, given analgesic and inoculated with C6 glioma cells (1×10^5 cells) *via* stereotaxic injection. CA was injected through a jugular catheter placed within 24 h of imaging. During each MRI procedure body temperature was maintained near 37 ˚C by a flow of warm air directed over the animal and respiration was monitored using a pneumatic pillow. Each rat was anesthetized using 2% isoflurane in oxygen for all surgical and imaging procedures. All experimental procedures were approved by Vanderbilt University's Institutional Animal Care and Use Committee.

DCE-MRI

While imaging procedures are described in more detail elsewhere (12), we briefly present the salient features. MRI was performed using a 9.4 T horizontal-bore magnet (Agilent, Santa Clara, CA, USA). A pre-contrast map of T_1 (i.e., T_{10}) was generated with data from an inversion-recovery snapshot experiment-repetition time (TR) = 12s, with 10 TIs logarithmically spaced between 0.250 and 11 s, two averaged excitations, 128 × 128 samples, 32 × 32 mm field of view prior to the injection of the CA. Two slices were acquired during the DCE-MRI experiment, one through the center of the brain tumor and another through the neck containing the major vessels feeding the brain. The DCE-MRI protocol consisted of a standard spoiled gradient-echo sequence with TR/TE/α = 10 ms/2.1 ms/15˚, a 96 × 96 acquisition matrix, and two averaged excitations; this protocol resulted in a temporal resolution of approximately 2 seconds. Dynamic images were collected before, during, and for 20 minutes after manually delivering a 200 µl bolus of 0.05 mmol kg^{-1} Gd–DTPA (Magnevist, Wayne, NJ) over 5 s.

Data Analysis

For each animal, the pre-contrast T_1 map was used to identify the tumor ROI from which an R_1 tissue time course was extracted for each voxel. This R_1 tissue time course is then related to C_t *via* Eq. [5], where $R_{10} \equiv 1/T_{10}$, and r_1 was assigned 3.8 $mM^{-1}s^{-1}$ (32). A (conservative) five to ten voxel ROI was then manually drawn around the linguofacial artery in the neck from which voxels exhibiting partial volume effects were eliminated by visual inspection and the remaining voxels were averaged to form the VIF. Using a model of fast water exchange (33) across red blood cell membranes, the R_1 time course of

the VIF was converted to C_p *via* Eq. [6], where blood R_{10} was assigned 0.435s^{-1} (34) and h was set to 0.46. After aligning the arrival times of the individual VIFs (VIF_{ind}), the mean of seven of the eight VIF_{ind} was used to create the population-averaged VIF (VIF_{pop}). Rat number two was excluded from the VIF_{pop} calculation for having a VIF_{ind} outside of one standard deviation from the calculated mean. Errors introduced by inflow effects were minimized through an iterative process based on the approach by Li *et al* (20). Briefly, each animal's VIF_{ind} and VIF_{pop} were scaled so that the concentration time course of a 50 voxel ROI in the temporalis muscle yielded a v_e of 0.11 (20,35,36). The scaled VIF_{ind} and VIF_{pop} for each animal were used with the C_t time courses from the tumor to extract K^{trans}, v_e, and v_p *via* both the ST and EX models through a non-linear fitting constrained to non-negative values in MATLAB R2012a (Natick, MA, USA). Additionally, the VIF_{pop} was then fit to Eq. [9] to generate a functional form of the VIF used in this study:

$$C_p(t) = a_1 \exp(-m_1 \cdot t) + a_2 \exp(-m_2 \cdot t), \quad [9]$$

where the summation of a_1 and a_2 refer to the amplitude of the first pass of CA and m_1 and m_2 refer to decay constants describing the washout of CA due to exchange with compartments and clearance through kidneys, respectively.

After fitting the voxel data to the ST and EX models the coefficient of determination, r^2, was calculated to measure the closeness of fit to the voxel data. Voxel fits with a returned $r^2 < 0.6$, or estimated parameters outside a physiologically relevant range ($0 < K^{trans} < 1$ min^{-1}, $0 < v_e < 1$, and $0 < v_p < 1$) were removed from subsequent analyses.

Statistical Analysis

Agreement between pharmacokinetic parameters determined by fitting C_t to the ST (K^{trans} and v_e) and EX (K^{trans},v_e, and v_p) models with both VIF_{ind} and VIF_{pop} were examined. The parameters estimated with VIF_{pop} ($K^{trans,pop}$, $v_{e,pop}$, and $v_{p,pop}$) and VIF_{ind} ($K^{trans,ind}$, $v_{e,ind}$, and $v_{p,ind}$) were paired (e.g., $K^{trans,ind}$ (ST) with $K^{trans,pop}$ (ST)) and compared at both the voxel and ROI levels. The paired data for each animal was then compared based on its Pearson correlation coefficient (PCC), concordance correlation coefficient (CCC), and by linear regression. Concordance correlation coefficients measures the agreement between two variables and was calculated using Eq. [10]

$$CCC = \frac{2 \cdot \sigma_{pop,ind}}{\sigma_{pop}^2 + \sigma_{ind}^2 + (\mu_{pop} - \mu_{ind})^2}, \qquad [10]$$

where σ_{pop} and μ_{pop} are the standard deviation and mean for a given parameter (e.g., K^{trans}, v_e, or v_p) estimated with VIF_{pop}, σ_{ind} and μ_{pop} are the standard deviation and mean for the same parameter estimated with both VIF_{ind}, and $\sigma_{pop,ind}$ is the covariance between the two variables (37). Confidence intervals for the individual voxel fits were calculated using *nlparci* (non-linear regression parameter confidence intervals) in MATLAB R2012a.

CHAPTER III

RESULTS

Population-averaged VIF

The population-averaged VIF is presented in Figure 4a (black line) where the gray lines represent one standard deviation from the population-averaged VIF. Both the peak and the washout share a similar standard deviation (19.0% and 18.1% of the mean, respectively). Figure 4b shows an example dynamic R_1 time course obtained from a single voxel along with the fit to the EX model using both the VIF_{ind} and VIF_{pop}.

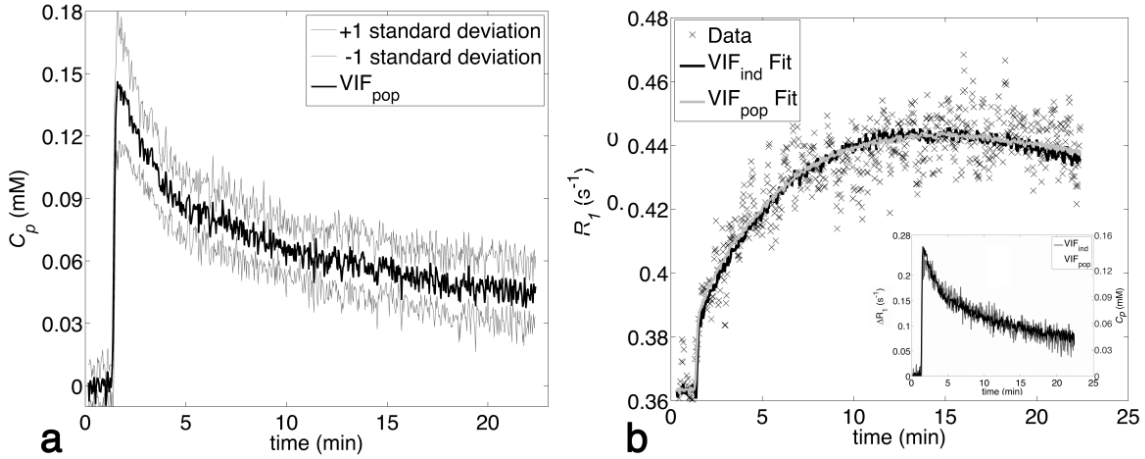

Figure 4. Panel **(a)** displays a population averaged VIF and the standard deviation at each time point; individual AIFs were tightly grouped resulting in a small difference between the standard deviations at the peak and during the washout period. Panel **(b)** shows an example voxel R_1 time course within a tumor fit with both the individual and population based VIFs, both of which show a good fit to the measured R_1 time course (r^2 = 0.8720 and 0.8780, respectively).

The inset in Figure 4b shows the population and individual based ΔR_1 ($\equiv R_{1b}(t)$-R_{10}) and C_p time courses for the VIF which were used for the EX and ST fitting. The VIF_{ind} and

VIF_{pop} based fits resulted in r^2 values of 0.8720 and 0.8780, respectively. The scaling factors used to minimize errors introduced by inflow effects for VIF_{ind} and VIF_{pop} were 3.3051 ± 1.0344 and 3.4554 ± 0.6552, respectively. Additionally the VIF_{pop} fitted to a bi-exponential model, Eq. [9], was described by a_1 = 0.0594 ± 0.0028 mM, m_1 = 0.5843 ± 0.0604 min^{-1}, a_2 = 0.0900 ± 0.0027 mM, and m_2 = 0.0369 ± 0.0027 min^{-1}.

ROI Analysis

The results of ROI analysis are presented in Figure 5a and Table 1. Fig. 5a is a combined plot of all ST and EX parameters estimated with VIF_{ind} (*y*-axis) plotted against the corresponding VIF_{pop} (*x*-axis) estimates for all animals. In these figures, the black lines represent the 45^o line while the individual points represent parameters from ROI fits and their respective 95% confidence intervals. The PCC provides a measurement of the strength of the linear relationship between parameters estimated using VIF_{pop} and VIF_{ind}, and may assume a value between -1 and 1. A PCC of 1 indicates a perfect positive linear correlation between the two groups, whereas a PCC of -1 indicates a perfect negative linear correlation. The groups are not linearly correlated if PCC is equal to zero. Similarly, CCC provides a measurement of the absolute agreement between parameters estimated using VIF_{pop} and VIF_{ind}, and may assume a value between 0 and 1. A CCC equal to 1 indicates perfect correlation, while a CCC equal to 0 indicates complete independence between the two groups. For the ROI analysis, a strong linear relationship was observed between parameters estimated using VIF_{pop} and VIF_{ind} with all parameters having PCCs greater than 0.8770. Additionally, ROI analysis resulted in CCCs greater than 0.8219 indicating a high level of correlation between VIF_{pop} and VIF_{ind} estimates of

both ST and EX parameters. ST estimates of K^{trans} and v_e had increased PCCs (PCC = 0.9783 and 0.9992) over EX estimates of K^{trans} and v_e (PCC = 0.9775 and 0.9985). Likewise, ST estimates of K^{trans} and v_e also had increased CCCs (CCC = 0.9565 and 0.9948) over EX estimates of K^{trans} and v_e (CCC = 0.9433 and 0.9941).

Table 1-CCC and Linear Regression for ROI Model Estimates

Parameter	CCC (95% CI)	PCC (95% CI)	Slope	Intercept
K^{trans} (ST)	0.9565 (0.9388 0.9742)	0.9783 (0.9718 0.9832)	1.1832[a]	-0.0002
v_e (ST)	0.9948 (0.9884 1.0012)	0.9992 (0.9990 0.9994)	1.0041	0.0001
K^{trans} (EX)	0.9433 (0.9234 0.9631)	0.9775 (0.9709 0.9827)	1.2555[a]	-0.0001
v_e (EX)	0.9941 (0.9872 1.0009)	0.9985 (0.9981 0.9989)	0.9928[a]	0.0001
v_p (EX)	0.8219 (0.7922 0.8516)	0.8770 (0.8429 0.9040)	1.2444[a]	-0.0001

[a]Slope significantly different from 1 ($P < 0.05$).

Voxel Analysis

The estimated parameters obtained by fitting the voxel level C_t time courses to the ST and EX models with both VIF_{ind} and VIF_{pop} were compared across all animals. Panel (b) in Figure 5 shows the voxel results of ST parameter K^{trans} estimated with the VIF_{ind} (y-axis) plotted against the VIF_{pop} (x-axis) estimated results for an individual animal. Panels (c)-(f) show similar data for the ST parameter v_e and EX parameters K^{trans}, v_e, and v_p.

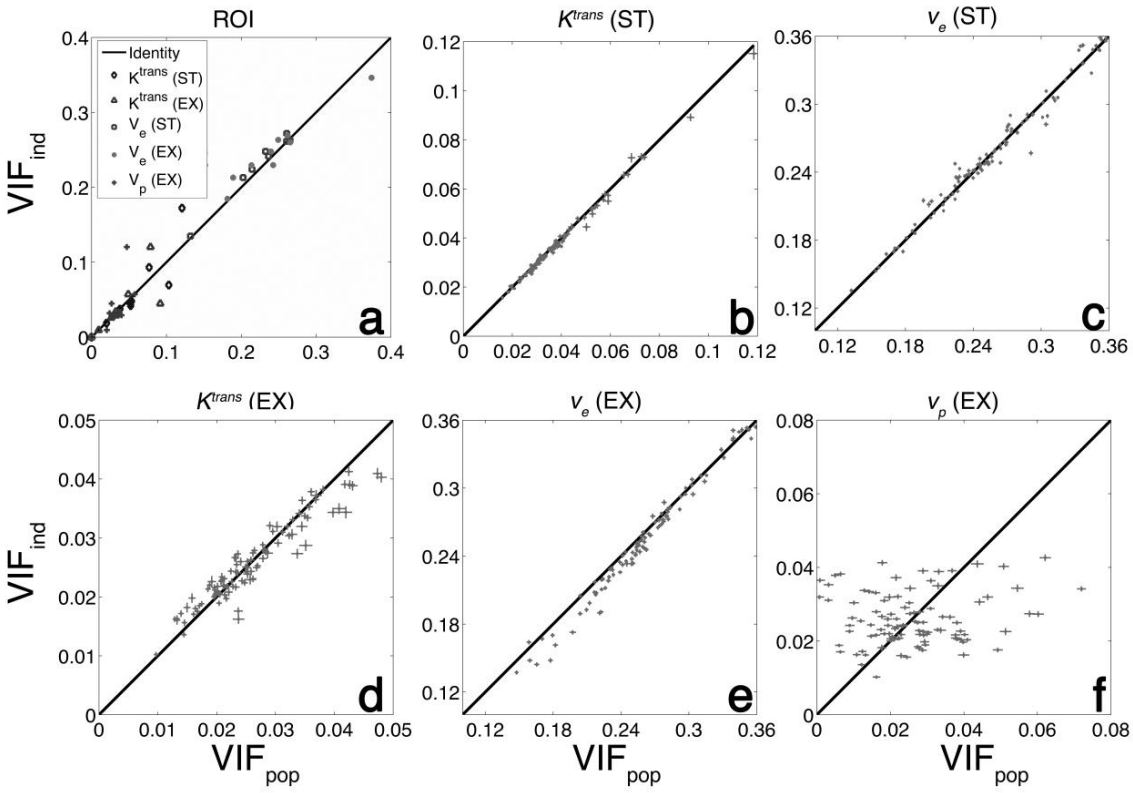

Figure 5. Estimates of pharmacokinetic parameters obtained from fitting dynamic data with the individual (*y*-axis) and population (*x*-axis) based VIFs. In these panels the black line represents the 45^{o} line while the individual points represent parameter values returned from voxel fits and their respective 95% confidence intervals. The results of ROI analysis for all parameters obtained from ST and EX models are displayed in panel **(a)**. PCCs and CCCs, displayed in Table 1, above 0.9783 and 0.9565 were observed for ST parameters, indicating a strong correlation and agreement between VIF_{ind} and VIF_{pop} estimated parameters. Specifically, both ST and EX estimates of v_e resulted in PCCs and CCCs greater than 0.9985 and 0.9941, respectively. Panels **(b-c)** represent the voxel level analysis for ST parameters, whereas panels **(d-f)** represent those obtained from the EX model. With the exception of v_p (EX), VIF_{pop} estimated parameters exhibited a strong linear relationship (PCC > 0.9159) with VIF_{ind} estimates.

The PCC along with its 95% confidence intervals computed for each animal and parameter are presented in Tables 2-3. ST and EX estimates of K^{trans} and v_e returned from voxel data analysis resulted in PCCs ranging from 0.9159 to 0.9965 indicating a strong linear relationship between the VIF_{ind} and VIF_{pop} estimated parameters. However, the v_p estimates using the individual and population based VIFs displayed a weaker linear

correlation, as seen in Fig. 5f and quantified with by the PCC value (PCC < 0.7174). The results of linear regression between the parameters returned from the VIF_{pop} and VIF_{ind} analyses are presented in Tables 2-3. The linear regression of ST model estimates of K^{trans} and v_e resulted in 13 of the 16 fits with slopes significantly different from one, whereas the EX model had 12 of 16 fits with slopes significantly different from one ($P < 0.05$). Likewise for intercept results, 10 of the 16 ST parameters and 14 of the 16 EX parameters had intercepts significantly different from zero ($P < 0.05$). Of the 25 slopes which were significantly different from zero, 11 were from overestimation of K^{trans} in fits using VIF_{pop} and seven were from underestimation of v_e in fits using VIF_{pop}.

Table 2-Linear Regression Results of Standard Model Voxel Estimates

Rat #	PCC (95% CI)		Slope		Intercept	
	K^{trans}	v_e	K^{trans}	v_e	K^{trans}	v_e
1	0.9870 (0.9810 0.9912)	0.9954 (0.9933 0.9969)	0.7192[a]	1.0806[a]	0.0044[b]	-0.0033
2	0.9802 (0.9716 0.9863)	0.9950 (0.9926 0.9965)	0.7948[a]	1.0422[a]	0.0046[b]	0.0010
3	0.9941 (0.9920 0.9957)	0.9939 (0.9917 0.9955)	0.8361[a]	1.0366[a]	0.0025[b]	0.0015
4	0.9872 (0.9820 0.9908)	0.9963 (0.9948 0.9974)	0.8797[a]	1.0311[a]	0.0012[b]	-0.0014
5	0.9917 (0.9870 0.9947)	0.9901 (0.9845 0.9937)	0.8612[a]	0.9825	0.0021[b]	0.0091[b]
6	0.9808 (0.9679 0.9885)	0.9960 (0.9934 0.9976)	1.3226[a]	1.0232	0.0125[b]	-0.0086[b]
7	0.9965 (0.9949 0.9976)	0.9886 (0.9832 0.9923)	0.9752[a]	0.9831	0.0004	0.0052
8	0.9924 (0.9901 0.9942)	0.9946 (0.9946 0.9968)	1.3664[a]	0.9248[a]	-0.0120[b]	0.0123[b]

[a]Slope significantly different from 1 ($P < 0.05$).
[b]Intercept significantly different from 1 ($P < 0.05$).

The high level of agreement observed in panels (b)-(f) of Figure 5 is quantified in Table 4 by the CCC and its 95% confidence interval. Visually, and confirmed in Tables

2-3, the ST estimates of K^{trans} and v_e (panels b-c) are more closely focused around the 45^o line than the EX estimates (panels d-e). For most rats, ST estimates of K^{trans} and v_e resulted in increased PCCs (16 of 16) and CCCs (15 of 16) over their EX model counterparts. Likewise, v_e (ST and EX) estimates had increased PCCs (11 of 16) and CCCs (13 of 16) over the K^{trans} (ST and EX) pair. A notable difference between the parameters estimated from the ST and EX models is the tighter confidence intervals for PCC and CCC values for ST parameters, while confidence intervals for v_p estimates are larger. 15 of 16 CCC confidence intervals obtained for K^{trans} (ST) and v_e (ST) are less than those for K^{trans} (EX) and v_e (EX). 13 of 16 PCC confidence intervals obtained for K^{trans} (ST) and v_e (ST) are also less than those for K^{trans} (EX) and v_e (EX). Similarly 15 of 16 CCC confidence intervals obtained for the ST and EX estimates of v_e are less than those for the ST and EX estimates of K^{trans}. 13 of 16 PCC confidence intervals obtained for the ST and EX estimates of v_e are also less than those for ST and EX estimates of K^{trans}. In general, a weak correlation (CCC < 0.6141) was observed between estimates of v_p estimated using VIF_{pop} and $VIF_{ind.}$ Although excluded from the VIF_{pop} calculation, both a strong linear relationship (PCCs > 0.9582) and strong agreement (CCCs > 0.8972) was observed for both ST and EX estimates of K^{trans} and v_e for rat number 2.

Table 3. Linear Regression Results of Extended Model Voxel Estimates

Rat #	PCC (95% CI)			Slope			Intercept		
	K^{trans}	v_e	v_p	K^{trans}	v_e	v_p	K^{trans}	v_e	v_p
1	0.9497 (0.9267 0.9657)	0.9637 (0.9468 0.9752)	0.5738 (0.4285 0.6901)	0.6307[a]	1.1254[a]	0.5328[a]	0.0084[b]	-0.0173[b]	0.0118[b]
2	0.9582 (0.9402 0.9708)	0.9811 (0.9728 0.9869)	0.2166 (0.0365 0.3831)	0.7407[a]	1.0018	0.2509[a]	0.0058[b]	0.0154[b]	0.0259[b]
3	0.9534 (0.9373 0.9655)	0.9732 (0.9638 0.9802)	0.4442 (0.3135 0.5584)	0.7403[a]	1.1073[a]	0.2620[a]	0.0061[b]	-0.0210[b]	0.0187[b]
4	0.9455 (0.9244 0.9609)	0.9603 (0.9448 0.9716)	0.5812 (0.4582 0.6824)	0.9507	0.9524[a]	0.2149[a]	0.0005[b]	-0.0118[b]	0.0050[b]
5	0.9818 (0.9717 0.9884)	0.9284 (0.8900 0.5370)	0.6048 (0.4429 0.7285)	0.9275[a]	1.0716	0.6116[a]	0.0043[b]	-0.0091	0.0113[b]
6	0.9538 (0.9235 0.9722)	0.9159 (0.8626 0.9491)	0.6102 (0.4216 0.7482)	1.1480[a]	0.9411	1.2204	0.0302[b]	0.0014	0.0631[b]
7	0.9539 (0.9326 0.9685)	0.9885 (0.9831 0.9922)	0.1190 (0.0753 0.3046)	0.7814[a]	1.0925[a]	0.0517[a]	0.0054[b]	-0.0300[b]	0.0245[b]
8	0.9215 (0.8991 0.9391)	0.9928 (0.9907 0.9945)	0.7174 (0.6475 0.7753)	1.2680[a]	0.9085[a]	0.4083[a]	-0.0048[b]	0.0064[b]	0.0337[b]

[a]Slope significantly different from 1 ($P < 0.05$).

[b]Intercept significantly different from 1 ($P < 0.05$).

Table 4. CCC Results for Standard and Extended Model Voxel Estimates

Rat #	CCC (95% CI) for Standard Model		CCC (95% CI) for Extended Model		
	K^{trans}	v_e	K^{trans}	v_e	v_p
1	0.8639 (0.8324 0.8954)	0.9522 (0.9394 0.9651)	0.8491 (0.8155 0.8828)	0.9046 (0.8762 0.9330)	0.5530 (0.5230 0.5831)
2	0.9001 (0.8751 0.9252)	0.9683 (0.9599 0.9766)	0.8972 (0.8707 0.9237)	0.9377 (0.9197 0.9557)	0.1741 (0.1612 0.1870)
3	0.9391 (0.9267 0.9515)	0.9752 (0.9694 0.9810)	0.9070 (0.8864 0.9275)	0.9521 (0.9403 0.9638)	0.3095 (0.2844 0.3347)
4	0.9679 (0.9600 0.9757)	0.9865 (0.9836 0.9894)	0.9386 (0.9198 0.9574)	0.9512 (0.9364 0.9659)	0.2223 (0.1904 0.2542)
5	0.9431 (0.9261 0.9601)	0.9721 (0.9633 0.9810)	0.9592 (0.9452 0.9732)	0.8862 (0.8448 0.9276)	0.5828 (0.5357 0.6300)
6	0.7852 (0.7219 0.8486)	0.9784 (0.9734 0.9834)	0.6931 (0.6070 0.7789)	0.8568 (0.7968 0.9167)	0.2018 (0.1471 0.2565)
7	0.9860 (0.9831 0.9889)	0.9790 (0.9721 0.9849)	0.9253 (0.9036 0.9469)	0.9696 (0.9614 0.9779)	0.0859 (0.0833 0.0886)
8	0.8805 (0.8621 0.8990)	0.9712 (0.9656 0.9767)	0.7847 (0.7470 0.8223)	0.9454 (0.9350 0.9558)	0.6141 (0.6064 0.6217)

CHAPTER IV

DISCUSSION AND CONCLUSIONS

A substantial challenge to performing quantitative DCE-MRI in small animals is the measurement of the VIF. While there are imaging and non-imaging approaches that can provide a reasonable estimate of the VIF, each method has its limitations. The necessity for high temporal resolution for imaging based estimates of the VIF significantly restricts the SNR, FOV, and spatial resolution available to characterize the tumor itself. Additionally, the small vessel size of laboratory animals may also constrain tumor implantation and imaging sites or require increasing the FOV to include a large blood pool. Finally, to better investigate tumor growth, angiogenesis, or treatment response multiple slice or 3D data sets are desired which will result in either a decreased spatial resolution and/or a FOV in order to maintain a temporal resolution appropriate for VIF estimation. One way to acquire multi-slice, high spatial resolution DCE-MRI data—without forfeiting a high temporal resolution VIF—is to use a population based VIF. This work has reported on the implementation and agreement between a population-averaged VIF and an individually acquired VIF in rats.

To address the overestimation of v_e observed in Skinner *et al* (12) a scaled VIF was used. One potential cause for v_e overestimation is the inflow effect on T_1-weighted images. Blood moving into the imaging slice which may not have fully experienced the previous RF excitation pulse results in an overestimation of the initial excited signal and, therefore, a decrease in the detection of a change in signal intensity. This inflow effect of

blood decreases the magnitude of the measured VIF resulting in an increased v_e as a result of overestimation of C_t. By using an iterative scaling process, we calibrated the measured VIF to a known v_e within the field of view (i.e., we assumed that the VIF should return a v_e of 0.11 for the temporal muscle (20,38). The reference tissue calibration allows for the underestimation of the VIF to potentially be corrected resulting in less overestimation of tissue v_e. Although similar to the reference region method, this approach does have one simplifying advantage to calibrating the VIF. The reference region approach relies on knowledge of the true value of both v_e and K^{trans} in the reference tissue, whereas, in the calibrated VIF approach, only knowledge of v_e is needed to calibrate the VIF. If only v_e is used in a reference region approach, then a three parameter fit is required (K^{trans} and v_e of the tissue of interest, as well as K_{trans} of the reference region) and these are well-known to be more unstable than two parameter fits. While it is true that K^{trans} could be used in either the calibration procedure or a reference region approach, estimates of K^{trans} for the reference tissue of (say) muscle vary considerably more than v_e and this would result in a systematic error in the K^{trans} estimates of the tissue of interest that scales approximately linearly with the error in the K^{trans} of the reference tissue (24). Thus, using v_e to "normalize" the VIF is a reasonable way forward that results in a numerically more stable fitting algorithm than a standard reference region approach. Additionally, the repeatability indices for K^{trans} and v_e (0.076 and 0.107, respectively) estimated using image derived VIFs are lower than those obtained for K^{trans} and v_e (0.222 and 0.204, respectively) through the reference region method (39,40). The decreased repeatability indices suggest that a VIF driven approach may be able to distinguish smaller statistically significant changes in K^{trans} and v_e.

The VIFs measured directly from the imaging data exhibited small (< 20%) standard deviations from the average VIF and is below the range previously reported in rats (11) and within the range observed in other studies (19,27). The minimal difference between the standard deviations at the peak concentration and the washout portions suggest that neither portions were more affected than the other by experimental (e.g., injection dose, injection rate) or physiological (e.g., heart rate, disease state, clearance rate) variability. The tight grouping of individual VIFs could account for the high correlation between K^{trans} (and v_e) values returned from analyses that employed the VIF_{pop} and VIF_{ind}.

The motivation of using a population-averaged over an individual VIF is the potential for high spatial resolution images to characterize tumor heterogeneity. Initially, high temporal resolution images are still needed to generate the VIF_{pop}, but future experiments using the resulting population based VIF benefit by the decrease in required temporal resolution and the increases in spatial resolution, and/or SNR, and/or FOV. Investigating tumor properties as a whole through ROI analysis, however, is a useful tool to capture overall tumor properties and can be used clinically to, for example, grade gliomas using extracted K^{trans} values (41). In this effort, ROI analysis of ST and EX estimates of K^{trans} and v_e suggests that using the VIF_{pop} provided parameters statistically similar, as observed by CCCs > 0.9433, to those produced with the VIF_{ind}. Compared to voxel estimates of v_p, the ROI estimates of v_p suggest that using VIF_{pop} provided increased similarity to VIF_{ind} parameters. This increase in similarity may arise from increased sensitivity of voxel fit parameters to deviations from the "true VIF". At the voxel level, if the VIF_{ind} was assumed to result in more accurate v_p estimates, the "true

VIF" would be more similar to the VIF_{ind} than the VIF_{pop}. At the ROI level the "true VIF" is a combination of the "true VIF" from every voxel and is more likely less biased towards the VIF_{ind} and approximately equally similar to both the VIF_{ind} and VIF_{pop}.

The results of this study also suggest that ROI and voxel estimates of v_e using the VIF_{pop} produced more statistically similar values and stronger linear relationships to VIF_{ind} estimates than estimates of K^{trans}. The increased agreement of v_e over K^{trans} in this study may be traced back to the use of a scaled VIF over an unscaled VIF. By calibrating VIF_{ind} and VIF_{pop} to a reference tissue's v_e, variations between VIF_{ind}'s and VIF_{pop}'s, specifically in washout amplitude, were decreased. Additionally, the higher PCC and CCC observed in ST model estimates over their EX model counterparts at both a voxel and ROI level, suggest either an increase sensitivity to variations between VIF_{pop} and VIF_{ind} due to the inclusion of the plasma space within the tissue space in Figure 3. The results of linear regression helped identify significant over- and underestimation of parameters estimated by VIF_{pop}. The over- and underestimation of these parameters, however, suggests that using VIF_{ind} and VIF_{pop} estimates to determine a precise tumor state may have differing results. However, if the over- or underestimation is consistent, the difference between two VIF_{ind} and VIF_{pop} measurements may exhibit the same trend. Additionally the fewer significant over- and underestimation of v_e compared to K^{trans} supports previous observations that VIF_{pop} produced stronger agreement to VIF_{ind} estimates.

Although using a population-averaged VIF may allow improved characterization of the tumor environment by reducing the temporal resolution and FOV constraints, it may not capture physiological differences between animals due to their disease

progression. In other studies experimental or physiological variation between animals was shown to effect VIF_{pop} estimates of model parameters (2626,29). However, assuming that experimental procedures remained consistent between animals, physiological variation did not seem to affect the degree to which VIF_{pop} estimated parameters agree with VIF_{ind} parameters.

To summarize, individual VIFs in eight rats were collected using an interleaved DCE-MRI procedure following an injection with Gd-DTPA. Using both the standard and extended models, pharmacokinetic parameters were extracted from fits using an individual VIF as well as the average of the individual VIFs (i.e., the population based VIF). The parameters estimated from the individual and population-averaged VIF based analyses were then compared. The results of this study indicate that both K^{trans} and v_e estimated using a population based VIF have a high level of agreement those estimated using an individual VIF. Thus, the use of a stringent injection protocol, ideally an automated syringe pump, we propose that individual vascular input functions can be obtained and combined to form a population vascular input function providing a suitable replacement for an individual VIF when one is not readily available.

Future Directions

The availability of measurements describing the molecular, cellular, and physiological characteristics of tumors provided by non-invasive imaging has increased in recent years. In particular, MRI and PET have matured to the point where they can provide noninvasive, quantitative, and 3D characterizations of, for example, blood flow, vessel permeability, blood volume, cellularity, hypoxia, metabolism, and cell

proliferation. One way to capitalize on the wealth of available information is to incorporate it into a realistic biophysical model of tumor growth that can be used to predict tumor growth and therapy response on an individual basis. By introducing imaging data into these models, terms requiring information available typically only by highly invasive methods (surgery, biopsy, or animal sacrifice) or within idealized (*in vitro*) systems can be replaced with terms supported by imaging data and then directly compared to *in vivo* tumor growth. One imaging method that can be used to populate the parameters in an appropriate model is DCE-MRI.

The goal of my current project is to incorporate quantitative multi-modality imaging into a biophysical model of tumor growth and treatment response. Using MRI and PET, data describing cellularity (diffusion weighted MRI, DW-MRI), proliferation (sequential DW-MRI data), blood volume fraction (DCE-MRI or quantitative blood oxygenation level dependent MRI, qBOLD-MRI), blood flow (DCE-MRI), oxygen saturation (qBOLD-MRI), and glucose concentration (FDG-PET) can be incorporated into a particular model of tumor growth. We hypothesize that high spatial resolution images are critical to the accuracy of this model, thus all the data—including DCE-MRI—needs to be acquired at the highest (reasonable) spatial resolution. The results of this current study support the development of a population-averaged VIF for use in quantitative DCE-MRI analysis. By using a population-averaged VIF over an individually acquired VIF, high temporal resolution can be traded for increased SNR, multiple slices, or increased spatial resolution. The result of which allows the incorporation of high spatial resolution DCE-MRI data into a model of tumor growth and angiogenesis. Incorporating data from MRI and PET into appropriate models of tumor

growth will potentially lead to a more pre-clinical and clinically relevant approach to tumor modeling that allows direct comparison between predicted and experimentally observed tumor characteristics.

REFERENCES

1. Folkman J, Bach M, Rowe JW, Davidoff F, Lambert P, Hirsch C, Goldberg A, Hiatt HH, Glass J, Henshaw E. Tumor Angiogenesis - Therapeutic Implications. New England Journal of Medicine 1971;285(21):1182-&.
2. Onishi M, Ichikawa T, Kurozumi K, Date I. Angiogenesis and invasion in glioma. Brain Tumor Pathology 2011;28(1):13-24.
3. Dvorak HF, Brown LF, Detmar M, Dvorak AM. Vascular-Permeability Factor Vascular Endothelial Growth-Factor, Microvascular Hyperpermeability, and Angiogenesis. American Journal of Pathology 1995;146(5):1029-1039.
4. Yankeelov TE, Gore JC. Dynamic contrast enhanced magnetic resonance imaging in oncology: Theory, data acquisition, analysis, and examples. Current Medical Imaging Reviews 2007;3(2):91-107.
5. Wedam SB, Low JA, Yang SX, Chow CK, Choyke P, Danforth D, Hewitt SM, Berman A, Steinberg SM, Liewehr DJ and others. Antiangiogenic and antitumor effects of bevacizumab in patients with inflammatory and locally advanced breast cancer. Journal of Clinical Oncology 2006;24(5):769-777.
6. Kim JK, Hong SS, Choi YJ, Park SH, Ahn H, Kim C-S, Cho K-S. Wash-in rate on the basis of dynamic contrast-enhanced MRI: Usefulness for prostate cancer detection and localization. Journal of Magnetic Resonance Imaging 2005;22(5):639-646.
7. Koh TS, Thng CH, Hartono S, Tai BC, Rumpel H, Ong AB, Sukri N, Soo RA, Wong CI, Low ASC and others. A comparative study of dynamic contrast-

enhanced MRI parameters as biomarkers for anti-angiogenic drug therapy. Nmr in Biomedicine 2011;24(9):1169-1180.

8. Evelhoch JL. Key factors in the acquisition of contrast kinetic data for oncology. Journal of Magnetic Resonance Imaging 1999;10(3):254-259.

9. Cheng H-LM. Improved correlation to quantitative DCE-MRI pharmacokinetic parameters using a modified initial area under the uptake curve (mIAUC) approach. Journal of Magnetic Resonance Imaging 2009;30(4):864-872.

10. Nagaraja TN, Karki K, Ewing JR, Divine GW, Fenstermacher JD, Patlak CS, Knight RA. The MRI-Measured Arterial Input Function Resulting From a Bolus Injection of Gd-DTPA in a Rat Model of Stroke Slightly Underestimates That of Gd-[(14)C]DTPA and Marginally Overestimates the Blood-to-Brain Influx Rate Constant Determined by Patlak Plots. Magnetic Resonance in Medicine 2010;63(6):1502-1509.

11. McGrath DM, Bradley DP, Tessier JL, Lacey T, Taylor CJ, Parker GJM. Comparison of Model-Based Arterial Input Functions for Dynamic Contrast-Enhanced MRI in Tumor Bearing Rats. Magnetic Resonance in Medicine 2009;61(5):1173-1184.

12. Skinner JT, Yankeelov TE, Peterson TE, Does MD. Comparison of dynamic contrast-enhanced MRI and quantitative SPECT in a rat glioma model. Contrast Media & Molecular Imaging 2012;7(6):494-500.

13. Pickup S, Chawla S, Poptani H. Quantitative Estimation of Dynamic Contrast Enhanced MRI Parameters in Rat Brain Gliomas Using a Dual Surface Coil System. Academic Radiology 2009;16(3):341-350.

14. Lee HB, Blaufox MD. Blood Volume in the Rat. Journal of Nuclear Medicine 1985;26(1):72-76.

15. Wedeking P, Eaton S, Covell DG, Nair S, Tweedle MF, Eckelman WC. Pharmacokinetic Analysis of Blood Distribution of Intravenously Administered Gd-153-Labeled Gd(Dtpa)2- and Tc-99m(Dtpa) in Rats. Magnetic Resonance Imaging 1990;8(5):567-575.

16. Su MY, Jao JC, Nalcioglu O. Measurement of Vascular Volume Fraction and Blood-Tissue Permeability Constants with a Pharmacokinetic Model - Studies in Rat Muscle Tumors with Dynamic Gd-DTPA Enhanced MRI. Magnetic Resonance in Medicine 1994;32(6):714-724.

17. Tofts PS, Kermode AG. Measurement of the blood-brain barrier permeability and leakage space using dynamic MR imaging. 1. Fundamental concepts. Magnetic Resonance in Medicine 1991;17(2):357-367.

18. Weinmann HJ, Laniado M, Mutzel W. Pharmacokinetics of Gd-DTPA Dimeglumine after Intravenous-Injection into Healthy Volunteers. Physiological Chemistry and Physics and Medical NMR 1984;16(2):167-172.

19. Parker GJM, Roberts C, Macdonald A, Buonaccorsi GA, Cheung S, Buckley DL, Jackson A, Watson Y, Davies K, Jayson GC. Experimentally-derived functional form for a population-averaged high-temporal-resolution arterial input function for dynamic contrast-enhanced MRI. Magnetic Resonance in Medicine 2006;56(5):993-1000.

20. Li X, Rooney WD, Varallyay CG, Gahramanov S, Muldoon LL, Goodman JA, Tagge IJ, Selzer AH, Pike MM, Neuwelt EA and others. Dynamic-contrast-

enhanced-MRI with extravasating contrast reagent: Rat cerebral glioma blood volume determination. Journal of Magnetic Resonance 2010;206(2):190-199.

21. Pathak AP, Artemov D, Bhujwalla ZM. Novel system for determining contrast agent concentration in mouse blood in vivo. Magnetic Resonance in Medicine 2004;51(3):612-615.

22. Paulus W, Peiffer J. Intratumoral Histologic Heterogeneity of Gliomas - A Quantitative Study. Cancer 1989;64(2):442-447.

23. Wagner M, Nafe R, Jurcoane A, Pilatus U, Franz K, Rieger J, Steinbach J, Hattingen E. Heterogeneity in malignant gliomas: a magnetic resonance analysis of spatial distribution of metabolite changes and regional blood volume. Journal of Neuro-Oncology 2011;103(3):663-672.

24. Yankeelov TE, Luci JJ, Lepage M, Li R, Debusk L, Lin PC, Price RR, Gore JC. Quantitative pharmacokinetic analysis of DCE-MRI data without an arterial input function: a reference region model. Magnetic Resonance Imaging 2005;23(4):519-529.

25. Just N, Koh DM, D'Arcy J, Collins DJ, Leach MO. Assessment of the effect of haematocrit-dependent arterial input functions on the accuracy of pharmacokinetic parameters in dynamic contrast-enhanced MRI. NMR in Biomedicine 2011;24(7):902-915.

26. Steingoetter A, Svensson J, Kosanke Y, Botnar RM, Schwaiger M, Rummeny E, Braren R. Reference Region-Based Pharmacokinetic Modeling in Quantitative Dynamic Contract-Enhanced MRI Allows Robust Treatment Monitoring in a Rat

Liver Tumor Model Despite Cardiovascular Changes. Magnetic Resonance in Medicine 2011;65(1):229-238.

27. Loveless ME, Halliday J, Liess C, Xu L, Dortch RD, Whisenant J, Waterton JC, Gore JC, Yankeelov TE. A quantitative comparison of the influence of individual versus population-derived vascular input functions on dynamic contrast enhanced-MRI in small animals. Magnetic Resonance in Medicine 2012;67(1):226-236.

28. Meng R, Chang SD, Jones EC, Goldenberg SL, Kozlowski P. Comparison between Population Average and Experimentally Measured Arterial Input Function in Predicting Biopsy Results in Prostate Cancer. Academic Radiology 2010;17(4):520-525.

29. Simpson NE, He ZQ, Evelhoch JL. Deuterium NMR tissue perfusion measurements using the tracer uptake approach: I. Optimization of methods. Magnetic Resonance in Medicine 1999;42(1):42-52.

30. Pickup S, Zhou R, Glickson J. MRI estimation of the arterial input function in mice. Academic Radiology 2003;10(9):963-968.

31. Kety SS. Peripheral blood flow measurement. Pharmacological Reviews 1951;3(1):1-41.

32. Rodriguez E, Roig A, Molins E, Arus C, Quintero MR, Cabanas ME, Cerdan S, Lopez-Larrubia P, Sanfeliu C. In vitro characterization of an Fe-8 cluster as potential MRI contrast agent. NMR in Biomedicine 2005;18(5):300-307.

33. Tofts PS, Brix G, Buckley DL, Evelhoch JL, Henderson E, Knopp M, Larsson HBW, Lee TY, Mayr NA, Parker GJM and others. Estimating kinetic parameters from dynamic contrast-enhanced T-1-weighted MRI of a diffusable tracer:

Standardized quantities and symbols. Journal of Magnetic Resonance Imaging 1999;10(3):223-232.

34. Dobre MC, Ugurbil K, Marjanska M. Determination of blood longitudinal relaxation time (T-1) at high magnetic field strengths. Magnetic Resonance Imaging 2007;25(5):733-735.

35. Donahue KM, Weisskoff RM, Parmelee DJ, Callahan RJ, Wilkinson RA, Mandeville JB, Rosen BR. Dynamic Gd-Dtpa Enhanced Mri Measurement of Tissue Cell-Volume Fraction. Magnetic Resonance in Medicine 1995;34(3):423-432.

36. Braren R, Curcic J, Remmele S, Altomonte J, Ebert O, Rummeny EJ, Steingoetter A. Free-Breathing Quantitative Dynamic Contrast-Enhanced Magnetic Resonance Imaging in a Rat Liver Tumor Model Using Dynamic Radial T-1 Mapping. Investigative Radiology 2011;46(10):624-631.

37. Lin LI. A Concordance Correlation-Coefficient to Evaluate Reproducibility. Biometrics 1989;45(1):255-268.

38. Fan XB, Haney CR, Mustafi D, Yang C, Zamora M, Markiewicz EJ, Karczmar GS. Use of a Reference Tissue and Blood Vessel to Measure the Arterial Input Function in DCEMRI. Magnetic Resonance in Medicine 2010;64(6):1821-1826.

39. Yankeelov TE, DeBusk LM, Billheimer DD, Luci JJ, Lin PC, Price RR, Gore JC. Repeatability of a reference region model for analysis of murine DCE-MRI data at 7T. Journal of Magnetic Resonance Imaging 2006;24(5):1140-1147.

40. Barnes SL, Whisenant JG, Loveless ME, Ayers GD, Yankeelov TE. Assessing the reproducibility of dynamic contrast enhanced magnetic resonance imaging in a murine model of breast cancer. Magnetic Resonance in Medicine 2012:n/a-n/a.

41. Zhang N, Zhang L, Qiu B, Meng L, Wang X, Hou BL. Correlation of volume transfer coefficient Ktrans with histopathologic grades of gliomas. Journal of Magnetic Resonance Imaging 2012;36(2):355-363.